DOI: 10.1002/adem.201300534

Magneto-Acoustic Mixing Technology: A Novel Method of Processing Metal-Matrix Nanocomposites**

By *Hunter B. Henderson, Orlando Rios, Zachary L. Bryan, Cody P. K. Heitman, Gerard M. Ludtka, Gail Mackiewicz-Ludtka, Alexander M. Melin* and *Michele V. Manuel**

With increasing concerns regarding fossil fuel consumption and the implementation of widespread vehicle lightweighting, light metal matrix nanocomposites (MMNC) are seen as an attractive solution in many industrial sectors including transportation and aerospace, which demand materials that simultaneously possess high strength and low weight.[1–4] However, processing of MMNCs to evenly disperse nanoparticles remains one of the great challenges to the advancement of this technology. Herein, we present a novel method for MMNC fabrication: magneto-acoustic mixing technology (MAMT). This technology uses ohmically decoupled static and alternating magnetic fields to produce high-intensity, non-contact sonication suitable for melt processing.[5] In this study, MAMT is used to disperse dysprosium oxide (Dy_2O_3) nanorods ($25 \times 225\,nm^2$) and erbium oxide (Er_2O_3) nanospheres (50 nm) in magnesium (Mg) in a high energy density acoustic environment. The resulting materials exhibit novel microstructures influenced by both acoustic and magnetic effects, which combine to break up nanoparticle agglomerations and refine microstructures. As this is the first demonstration of this technology, the versatility of MAMT is highlighted, and its far-reaching impact will be discussed.

Ceramic nanoparticle reinforcement of light metals has been extensively evaluated and shown to broadly improve mechanical properties such as strength, toughness, creep resistance, and elastic modulus.[6–8] While nanoparticle reinforcement is desirable, reliable incorporation has proven to be the fundamental challenge to MMNC production, as high surface energies drive particles to agglomerate.[6] When agglomerations are present in the fabricated microstructure, they act as crack nucleation sites, degrading material properties.[9] Melt dispersion methods like horn-based sonication, powder metallurgy, and spray forming have previously been used to disperse nanoparticles, but MAMT presents the opportunity to disperse nanoparticles using a non-contact, bulk processing technique. MAMT is distinct from other electromagnetic mixing, vibration or sonication technologies[10,11] because of its processing flexibility, deriving from the ohmically decoupled system. This facilitates independent control over many of the processing variables, enabling the production of alloys that do not suffer from many of the issues associated with more traditional melt processing technologies, such as contamination from melt-transducer interactions,[12] restricted geometries, and limited interaction volumes.[13]

1. Theoretical

The MAMT process is shown schematically in Figure 1a and b. In the current experimental set-up, an induction coil serves two purposes. First, the induced alternating eddy currents heat the sample by Joule heating. Second these electric currents interact with an additional perpendicular static magnetic field to produce an alternating Lorentz force in the sample, leading to acoustic effects and melt sonication. The distribution of induction currents is of primary importance to the process, and is described by a surface-dominated

[*] *Prof. M. V. Manuel, H. B. Henderson, Z. L. Bryan, C. P. K. Heitman*
University of Florida, 100 Rhines Hall, P.O. Box 116400, Gainesville, FL 32611, USA
E-mail: mmanuel@mse.ufl.edu
Dr. O. Rios, Dr. G. Mackiewicz-Ludtka, Dr. G. M. Ludtka, Dr. A. M. Melin
Oak Ridge National Laboratory, 1 Bethel Valley Road, Oak Ridge, TN 37831, USA

[**] *The authors acknowledge the National High Magnetic Field Laboratory, Tallahassee, FL, for the generous use of their DC magnet facilities and the Manufacturing Demonstration Facility at Oak Ridge National Laboratory for providing sample handing and electromagnetic processing apparatus. This material is based upon work supported by the National Science Foundation under grant numbers DMR-0845868 and IRES-1129412. The research sponsored was in part by the U.S. Department of Energy, Office of Energy Efficiency and Renewable Energy, Advanced Manufacturing Office, under contract DE-AC05-00OR22725 with UT-Battelle, LLC. Additionally, the authors acknowledge assistance by Dr. Quadir Zakaria at the Electron Microscopy Unit of the University of New South Wales with their assistance with the EBSD. Additionally, the authors would like to thank Professor Gregory Thompson and the Central Analytical Facility at the University of Alabama-Tuscaloosa in their assistance with TEM (Supporting Information is available online from Wiley Online Library or from the author).*

 © 2014 WILEY-VCH Verlag GmbH & Co. KGaA, Weinheim

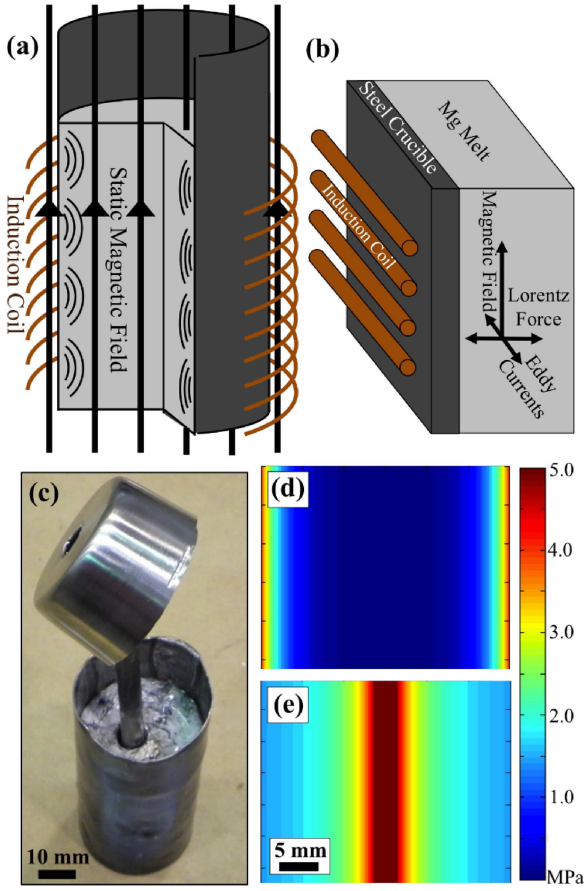

Fig. 1. (a) Schematic of the MAMT showing orientation of the static magnetic field through crucible and sample. (b) Close-up view of (a) in which induction eddy currents in the sample interact with a static magnetic field by the Lorentz force to produce driven oscillations (10 kHz in this investigation) and sonic power. (c) Photograph of a sample prior to MAMT. The rod in the center is a stainless steel thermocouple sleeve used to monitor temperature during processing. Cross-section of the acoustic pressure in the sample based on (d) acoustic production, and (e) combined production and propagation.

mechanism known, as the skin effect in:[14]

$$J(d) = J_s e^{-d/\delta}, \delta = \sqrt{\frac{\rho}{\pi f \mu_0 \mu_r}} \quad (1)$$

where $J(d)$ is the current density, J_s is the surface current density, d is distance inward from the crucible edge, δ is the skin depth, ρ is the material resistivity, f is the induction frequency, μ_0 is vacuum permeability, and μ_r is the material relative permeability. The skin effect is caused by internally opposing current loops generated by an alternating current, and 63% of the induction current is contained within the skin depth.[14] By applying a high magnetic field, smaller alternating currents may be used to generate vibrations, and thus sonication, while maintaining control over Joule heating. In the current study, only 8.6% of the current is calculated to be within the crucible, thus the melt is sonicated directly. Through manipulation of relationships between electromagnetic vibration (EMV) particle acceleration[11] and acoustic pressure,[15] the distribution of acoustic pressure in the melt may be calculated by:

$$p_{ac}(d) = \frac{I_{in} B c}{2\pi f h_w \delta} e^{-d/\delta} \quad (2)$$

where, for the current set-up, I_{in} is the total induced current (700 A), B is the static magnetic field strength (20 T), c is the speed of sound (3935 m s^{-1} in liquid Mg[16]), h_w is the height of the crucible (80 mm), and δ is the skin depth (2.5 mm in liquid Mg at 10 kHz). This relationship was used to produce Figure 1d.

The previous equation for acoustic pressure, however, does not take propagation of acoustic waves into account. The pressure in a cylindrical wave increases away from the source by geometric amplification according to:

$$\frac{p}{p_0} = \left(\frac{R}{R-d}\right)^{0.45} \quad (3)$$

where p is the pressure at an inward radial distance d, p_0 is the source pressure, and R is the radius.[17] By this model, the theoretical pressure approaches infinity at the central axis, but the pressure is limited by the mean free path of the oscillating liquid atoms and is finite.[13] This model also does not account for attenuation of acoustic intensity. The pressure distribution in the melt is combined with the acoustic production model in Figure 1e. The resulting distribution of acoustic pressure indicates that the entire sample undergoes acoustic cavitation while molten, since the entire sample is above the cavitation threshold of 0.5–1.0 MPa for light metals.[11]

In MAMT, both acoustic and magnetic mechanisms can affect the resulting structures. The most striking acoustic effects are due to cavitation, during which local conditions can exceed 100 atm and 5000 K.[18] Acoustic solidification processing is widely used in metal casting to degas melts[19] and refine cast microstructures.[13,20] Grain refinement is due to more efficient heat transfer between the melt and solidification front and remelting of dendrite arms, both of which increase the number density of crystal nuclei.[15] In the case of MMNC processing, cavitation is theorized to hinder nanoparticle agglomeration.[21,22] Acoustic streaming, enhanced convection by added buoyancy of cavitation bubbles, also induces local remelting of dendrite arms, thereby limiting dendritic growth.[23] In addition to acoustic effects, high-strength magnetic fields concurrently contribute additional mechanistic features. For example, crystals can become oriented in the field by magnetocrystalline anisotropy and/or magnetic shape anisotropy,[24,25] producing textured microstructures otherwise unachievable by casting.[26] Magnetohydrodynamic interactions also reduce convection of a conductive melt[27] and can inhibit particle motion through the fluid.[28] While magnetic effects would tend to decrease convection, acoustic effects, in the form of acoustic streaming, would act to increase it.

 © 2014 WILEY-VCH Verlag GmbH & Co. KGaA, Weinheim

2. Experimental Section

The base materials were 99.8% Mg extruded rod from Strem Chemical and $30 \times 225\,nm^2$ Dy_2O_3 rods and 50 nm Er_2O_3 spheres supplied by Nanostructured and Amorphous Materials, Inc. Pre-processing of the samples involved melting the Mg rod in a stainless steel crucible (0.5 mm wall thickness) under argon (Ar), followed by solidification around a stainless steel thermocouple sleeve. Holes were then drilled in the solidified Mg, which were filled with 1 vol% nanoparticles, and capped with 99.99% Mg slugs obtained from Alfa Aesar.

MAMT processing was performed at the National High Magnetic Field Laboratory under a 20 T Bitter magnet in an experimental set-up designed to withstand high sonication energies.[5] A specialized set-up, including crucible support, an induction coil, and Ar and helium (He) flow was used inside the bore of the magnet to apply MAMT power. Sample temperature was measured by a K-type thermocouple enclosed in the thermocouple sleeve. First, under Ar, the induction coil heated a stainless steel crucible containing the sample past the Mg melting temperature to 700 °C. Subsequently, the static magnet ramped to 20 T, during which the acoustic pressure at the crucible wall was 3.9 MPa. The sample was held at full power for 5 min, after which a flow of He quenched the sample while MAMT power was continually delivered. The sample solidified and was cooled to finish the process.

Optical micrographs were collected on a Leica DM2500 and grain size was collected using a standard linear intercept method (ASTM E112). Error bars in Figure 2b are 1σ and are within the line thickness at small grain sizes. Electron backscatter diffraction (EBSD) studies were conducted on a Zeiss Auriga CrossBeam Workstation with a NordlysF detector at the Electron Microscope Unit at the University of New South Wales. The accelerating voltage was 20 kV and the EBSD step size was 4 μm. Transmission electron microscopy (TEM) was performed on a FEI Technai in operating at 200 kV at the Central Analytical Facility at the University of Alabama-Tuscaloosa. Samples were prepared by standard FIB cross-section techniques[29] and imaged in scanning transmission electron microscopy high angle annular dark field (STEM-HAADF) mode. Radiography was conducted with a Cu X-ray source at 250 kV and 120 μA at a resolution of 50 μm and a digital flat panel detector.

3. Results and Discussion

The samples investigated in the present work are Mg (99.8% purity) with either 1 vol% $25 \times 225\,nm^2$ (nominal) Dy_2O_3 nanorods or 1 vol% 50 nm Er_2O_3 nanospheres. Mg was chosen because of the potential to develop microstructural texture due to magnetic anisotropy inherent in the HCP crystal structure, as well as it technological relevance,[30]

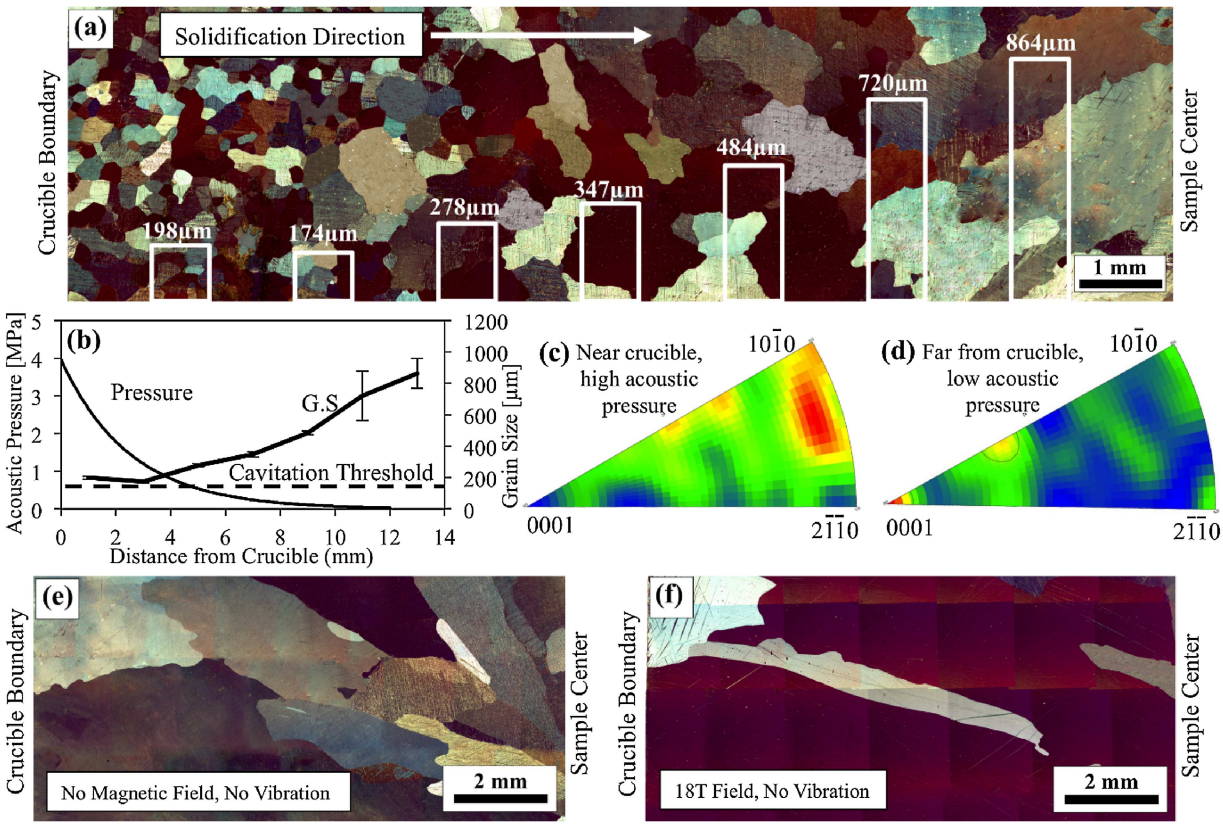

Fig. 2. (a) Microstructure of MAMT-cast Mg-1 vol% Dy_2O_3 from the crucible edge (left) to the center of the cylinder (right), with corresponding grain size. (b) Grain size and acoustic pressure as a function of distance from the crucible. (c) and (d) Inverse pole figure by EBSD of areas near the crucible wall and near the center of the sample, respectively. Microstructures of comparable Mg samples are presented solidified (e) with no magnetic field or sonication and (f) with an 18 T field but no sonication.

 © 2014 WILEY-VCH Verlag GmbH & Co. KGaA, Weinheim

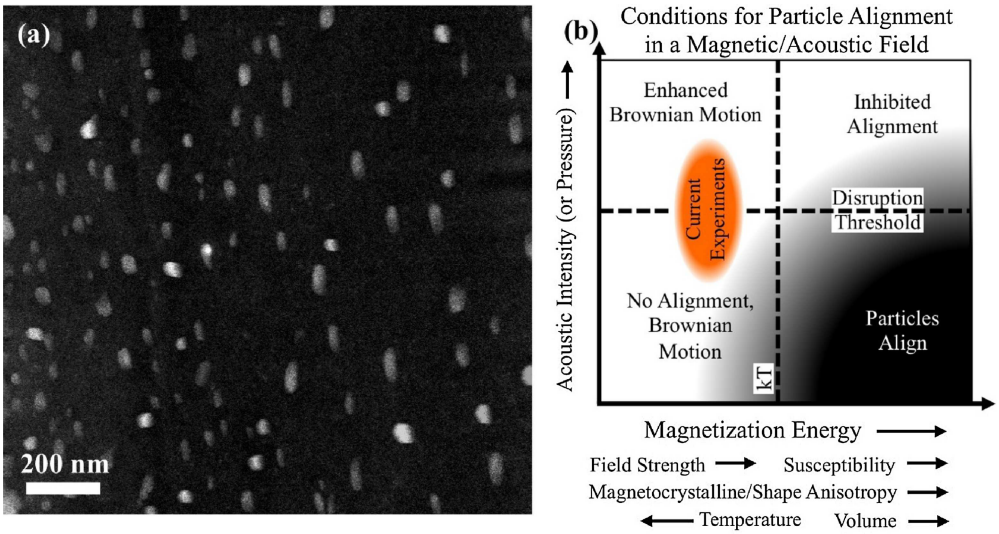

Fig. 3. Distribution and alignment of anisotropic particles. (a) annular dark field scanning transmission electron microscope (ADF-STEM) micrographs of MAMT-treated Mg reinforced with Dy_2O_3 nanoparticles. (b) Conceptual map of the conditions under which magnetic alignment of particles suspended in a liquid during acoustic treatment may be expected, along with contributing factors.

Dy_2O_3 and Er_2O_3 were selected because of their greater (more negative) free energy of formation compared to MgO[31] and consequent thermodynamic stability in molten Mg. Additionally, rare-earth oxides exhibit high magnetic susceptibilities,[32] which in the presence of the strong static field is expected to aid in dispersion and potential alignment of the particles.[33]

The microstructure of MAMT-cast Mg-Dy_2O_3 is shown in Figure 2a. A transition from small (compared to typical Mg cast grain size,[34] seen in Figure 2e) equiaxed grains near the crucible to progressively coarser grains toward the center is evident. Seen in Figure 2b, the transition to coarser grains is a result of exponential decay of acoustic pressure (Equation 2) away from the crucible, a consequence of the skin effect. The grain size increases towards the center of the sample because, as solidification progresses inward from the crucible, acoustic production becomes less efficient in the solid material. This effect is not due to traditional heat transfer, since the solidification front velocity increases away from the edge of the sample for 30 mm cylindrical samples.[35] If this mechanism were dominant, grain size would decrease near the center of the sample. Texture effects are also observed. Specifically, the anisotropic Mg grains basally orient toward the field (in the measured orientation, basal-field alignment is indicated by (0001) intensity) more strongly at lower acoustic intensities (Figure 2d compared to 2c). Disordering acoustic forces would tend to be less intense away from the crucible wall, increasing basal alignment. The image plane for both samples was perpendicular to the magnetic field direction. MAMT-induced dispersion of Dy_2O_3 nanorods is shown in Figure 3a. It is noted that any apparent alignment in Figure 3a may be attributed to rotation prior to engulfment by the solidification front. The conditions under which the asymmetric (by shape or crystallography) particles would be expected to align are shown in Figure 3b, thus the particles are not expected to align in the current set-up. High temperature (1000 K) and small particle volume are largely responsible for the low demagnetization energies.

Figure 4a and b illustrate the macroscopic distribution of particles in Mg-1% 50 nm Er_2O_3 processed samples with and without MAMT, respectively, using X-ray radiography. The particles were initially inserted into a tubular opening created in a solid Mg block prior to MAMT and remained unaltered by melting, seen in Figure 4b. Figure 4a displays a sample halted partway through MAMT process illustrating a snapshot in

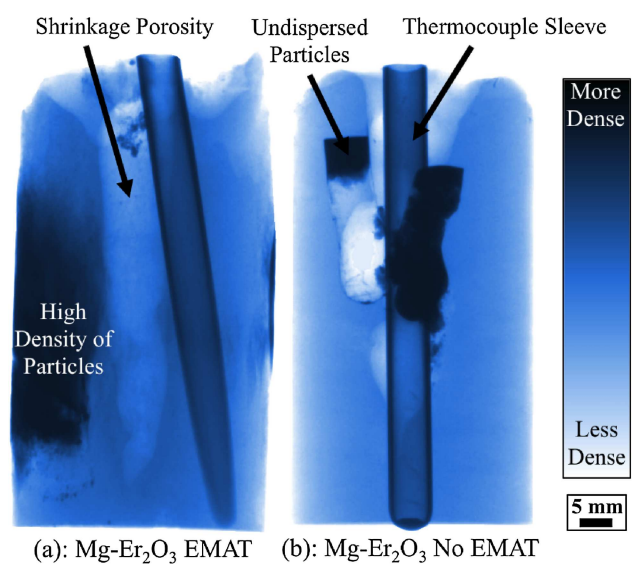

Fig. 4. Effect of MAMT on macro-scale dispersion of particles. X-ray radiography of Mg-Er_2O_3 composites (a) processed with MAMT to partially disperse particles and (b) melted with no acoustic power, showing minimal dispersal. The particles appear darker than the Mg matrix. The particles were initially inserted through a cylindrical drilled out hole in a pure Mg ingot prior to MAMT processing. Thus, the sample with no acoustic power contains particles in nearly the same shape as its initial placement into the Mg ingot prior to MAMT processing. A central shrinkage pipe and a steel thermocouple sleeve are visible in both samples.

 © 2014 WILEY-VCH Verlag GmbH & Co. KGaA, Weinheim

time of the dynamic nature of the redistribution of particles from a central location. Figure 4a was chosen since even distribution of nanoparticles is difficult to resolve using X-ray radiography due to the fine scale of the particles.

A key aspect of MAMT is the ability to adjust the process broadly, depending on the desired structure. Sonication frequency, static magnetic flux density, and solidification speed are independently variable. The sonication intensity scales with both the field and induction power and is thus controllable by either. The induction skin depth, and consequent region sonicated, is dependent on the properties of the crucible and the applied induction frequency. To operate MAMT in crucible sonication mode, as opposed to vibrating the melt, higher frequencies and a more conductive or ferromagnetic crucible could be used.

4. Conclusions

In summary, MAMT has been demonstrated as a potential method of fabricating MMNCs. The sonication mode is dependent on the skin depth of induction eddy currents, and can function as either crucible or melt sonication, depending on the fraction of current in the crucible. The current studies were in a melt sonication mode. Both microstructural refinement and particle dispersion by acoustic processes were demonstrated. The potential applications of MAMT are far-reaching. The experimental set-up may be adapted to casting of net-shape parts, following melt particle dispersion by MAMT. The MAMT process may also be well suited to continuous, high-throughput processes where a melt is continually processed through an MAMT zone. The non-contact nature of MAMT is favorable for biomedical and aerospace applications that require high-purity materials, since it avoids sonicating horn erosion.[12] Processes that benefit from external magnetic fields and acoustic energy, such as sonochemistry and precipitation modification, are especially promising future applications.

Received: November 22, 2013
Final Version: January 31, 2014
Published online: January 01, 2013

[1] W. J. Joost, *JOM* **2012**, *64*, 1032.
[2] V. Viswanathan, T. Laha, K. Balani, A. Agarwal, S. Seal, *Mater. Sci. Eng. R-Rep.* **2006**, *54*, 121.
[3] G. P. Cao, H. Konishi, X. C. Li, *J. Manuf. Sci. Eng.-Trans. ASME* **2008**, *130*, 6.
[4] J. B. Ferguson, F. Sheykh-Jaberi, C. S. Kim, P. K. Rohatgi, K. Cho, *Mater. Sci. Eng. A-Struct. Mater. Prop. Microstruct. Process* **2012**, *558*, 193.
[5] R. K. R. Jaramillo, Ge. Ludtka, Ga. Ludtka, J. Wilgen, *USA Patent US7534980 B2*, **2009**.
[6] S. C. Tjong, *Adv. Eng. Mater.* **2007**, *9*, 639.
[7] S. C. Tjong, Z. Y. Ma, *Mater. Sci. Eng. R-Rep.* **2000**, *29*, 49.
[8] H. Dieringa, *J. Mater. Sci.* **2011**, *46*, 289.
[9] K. B. Nie, X. J. Wang, L. Xu, K. Wu, X. S. Hu, M. Y. Zheng, *J. Alloy. Compd.* **2012**, *512*, 355.
[10] C. Vivés, *Mater. Sci. Eng. A-Struct. Mater. Prop. Microstruct. Process.* **1993**, *173*, 169.
[11] C. Vivés, *Metall. Mater. Trans. B-Proc. Metall. Mater. Proc. Sci.* **1996**, *27*, 445.
[12] S. Komarov, D. Kuznetsov, *Int. J. Refract. Metals Hard Mater.* **2012**, *35*, 76.
[13] M. Qian, A. Ramirez, A. Das, *J. Cryst. Growth* **2009**, *311*, 3708.
[14] H. W. Deng, Y. J. Zhao, C. J. Liang, W. S. Jiang, Y. M. Ning, *Prog. Electromagn. Res. M* **2009**, *9*, 1.
[15] G. I. Eskin, *Ultrasonic Treatment of Light Alloy Melts*, Gordon and Breach Science Publishers, Amsterdam **1998**.
[16] S. Sengul, D. J. Gonzalez, L. E. Gonzalez, *J. Phys.-Condes. Matter* **2009**, *21*, 11.
[17] F. Winterberg, *The Release of Thermonuclear Energy by Inertial Confinement: Ways Toward Ignition*, World Scientific Publishing Company, Hackensack, NJ **2010**.
[18] H. G. Flynn, *J. Acoust. Soc. Am.* **1975**, *58*, 1160.
[19] G. I. Eskin, *Ultrason. Sonochem.* **1995**, *2*, S137.
[20] M. J. Li, T. Tamura, N. Omura, K. Miwa, *Trans. Nonferrous Met. Soc. China* **2010**, *20*, 1192.
[21] Y. Yang, J. Lan, X. C. Li, *Mater. Sci. Eng. A-Struct. Mater. Prop. Microstruct. Process.* **2004**, *380*, 378.
[22] G. Cao, J. Kobliska, H. Konishi, X. Li, *Metall. Mater. Trans. A-Phys. Metall. Mater. Sci.* **2008**, *39A*, 880.
[23] O. V. Abramov, *Ultrasonics* **1987**, *25*, 73.
[24] J. A. Osborn, *Phys. Rev.* **1945**, *67*, 351.
[25] C. Y. Wu, S. Q. Li, K. Sassa, Y. Chino, K. Hattori, S. Asai, *Mater . Trans.* **2005**, *46*, 1311.
[26] M. J. Li, T. Tamura, K. Miwa, *Metall. Mater. Trans. A-Phys. Metall. Mater. Sci.* **2009**, *40A*, 1422.
[27] S. Yang, W. J. Liu, J. Jia, *J. Mater. Sci.* **2001**, *36*, 5351.
[28] S. Asai, *Model. Simul. Mater. Sci. Eng.* **2004**, *12*, R1.
[29] R. M. Langford, A. K. Petford-Long, *J. Vac. Sci. Technol. A-Vac. Surf. Films* **2001**, *19*, 2186.
[30] M. K. Kulekci, *Int. J. Adv. Manuf. Technol.* **2008**, *39*, 851.
[31] M. Binnewies, E. Milke, *Thermochemical Data of Elements and Compounds*, Wiley-VCH, New York **2002**.
[32] H. B. Lal, V. Pratap, A. Kumar, *Pramana* **1978**, *10*, 409.
[33] Q. A. Wang, T. Liu, K. Wang, C. J. Wang, K. Nakajima, J. C. He, *ISIJ Int.* **2010**, *50*, 1941.
[34] C. H. Caceres, G. E. Mann, J. R. Griffiths, *Metall. Mater. Trans. A-Phys. Metall. Mater. Sci.* **2011**, *42A*, 1950.
[35] J. Gammon, J. A. Howarth, *Int. Commun. Heat Mass Transf.* **1996**, *23*, 387.

 © 2014 WILEY-VCH Verlag GmbH & Co. KGaA, Weinheim